Lithium Tritelluride as an Electrolyte Additive for Stabilizing Lithium Deposition and Enhancing Sulfur Utilization in Anode-free Lithium-sulfur Batteries

*Tianxing Lai, Amruth Bhargav, and Arumugam Manthiram**

T. Lai, Dr. A. Bhargav, Prof. A. Manthiram
Materials Science & Engineering Program and Texas Materials Institute, The University of Texas at Austin, Austin, TX, 78721 USA
E-mail: rmanth@mail.utexas.edu

Keywords: lithium-sulfur batteries, anode-free cells, electrolyte additive, lithium anode protection, cathode kinetics

Despite the potential to become the next-generation energy storage technology, practical lithium-sulfur batteries are still plagued by the poor cyclability of lithium-metal anode and sluggish conversion kinetics of S species. In this study, lithium tritelluride ($LiTe_3$), synthesized with a simple one-step process, is introduced as a novel electrolyte additive for lithium-sulfur batteries. $LiTe_3$ quickly reacts with lithium polysulfides and functions as a redox mediator to greatly improve the cathode kinetics and the utilization of active materials in the cathode. Moreover, the formation of a Li_2TeS_3/Li_2Te-enriched interphase layer on the anode surface enhances ionic transport and stabilizes Li deposition. By regulating the chemistry on both the anode and cathode sides, this additive enables a stable operation of anode-free lithium-sulfur batteries with only 0.1 M concentration in conventional ether-based electrolytes. The cell with the $LiTe_3$ additive retains 71% of the initial capacity after 100 cycles, while the control cell retains only 23%. More importantly, with a high utilization of Te, the additive enables significantly better cyclability of anode-free pouch full-cells under lean electrolyte conditions.

1. Introduction

As the global market for clean and renewable energy continuously grows, there is a greater demand for groundbreaking energy storage devices that can outperform current lithium-ion technology. Lithium-sulfur (Li-S) batteries are considered as one of the most promising candidates for next-generation energy storage systems, owing to their high energy density (2,600 W h kg^{-1}), large specific capacity (1672 mA h g^{-1}), and low cost of elemental sulfur.[1, 2] Conventional Li-S cell feature two key processes: (i) solid-liquid-solid conversion of sulfur species, from S to intermediate lithium polysulfide (LiPS) to the discharge end product Li_2S; (ii) Li stripping and plating on the anode side. However, the kinetics of sulfur species conversion is sluggish due to the insulating nature of S/Li_2S and solvation structure of LiPS in the electrolyte. Additionally, LiPS can migrate to the Li anode and form an unstable solid-electrolyte interphase (SEI) layer through the notorious polysulfide shuttle effect, resulting in rapid Li anode degradation, electrolyte decomposition, and active material loss. These crucial problems, among others, impede the practical application of Li-S batteries.[3, 4]

Numerous efforts have been devoted to overcoming these challenges in the Li-S systems. Due to the intrinsically low stripping and plating efficiency of Li and corrosion from LiPS, Li-metal anode is not stable in Li-S cells, which consequently leads to the requirement for excess Li and electrolyte.[5] Different methods to modify the cathode architecture have been developed to mitigate LiPS shuttling and catalyze sulfur species conversion.[6-12] Li anode engineering and protection strategies like artificial SEI have also demonstrated their ability to stabilize Li deposition in Li-S batteries.[13-20] However, these techniques generally require sophisticated synthesis processes. Recently, a new approach was introduced by our group to dramatically improve the cyclability of Li-metal anode by constructing a ternary sulfide-rich SEI layer ($Li_aX_bS_c$).[21, 22] In particular, by adding elemental Te in the cathode, lithium polytellurosulfide species could be formed, which can migrate to the anode and deposit a Li_2TeS_3-containing SEI

layer to help reversibly cycle Li anode. This method cleverly exploits the seemingly detrimental shuttle effect to limit Li loss, extending the lifespan of Li-limited or anode-free Li-S batteries (using Ni foil as the anode current collector and commercial Li_2S as the cathode active material). Despite its success, the utilization of Te was limited, requiring a relatively large amount of Te, which negatively impacts the energy density and cost efficiency of the cells.

Meanwhile, the area of designing electrolyte additives for Li-S batteries to mitigate the shuttle effect and protect Li anode is promising, yet less explored.[23, 24] $LiNO_3$ is a commonly used additive for ether-based electrolytes in Li-S batteries. It can passivate Li surface by converting the precipitating reduced sulfide species to oxidized sulfate species ($Li_2S_xO_y$), forming a relatively stable SEI layer.[25] However, this layer exhibits poor Li-ion conductivity and progressively increasing resistance as the cell cycles and the nitrate is depleted. Other electrolyte additives, including lithium iodide, phosphorous pentasulfide, tin iodide, etc., also show their ability to generate an effective protection layer on Li anode, but the stability and ionic conductivity of the formed SEI layer, as well as the cyclability and efficiency of the cell, could be further improved.[26-29]

Inspired by these aspects, we herein present lithium tritelluride ($LiTe_3$) as a novel electrolyte additive to tune the reaction kinetics in Li-S cells and introduce a protective SEI layer on the surface of the electrodes. We find that this additive can improve both the Li anode stability and the cathode kinetics. At the Li_2S cathode, $LiTe_3$ greatly reduces the activation barrier of Li_2S and promotes the kinetics of sulfur species conversion by generating polytellurosulfides as redox mediators. The polytellurosulfides then migrate and get reduced on the anode to form a Te-enriched SEI layer. The Li plating and stripping efficiency is clearly enhanced with this SEI structure. Anode-free Li-S full cells show significantly better cyclability and improved capacity. Even in a practical, lean electrolyte pouch full cell configuration, this additive still displays its effectiveness with a high utilization of Te.

2. Results and discussion

2.1 Synthesis

As discussed in the introduction, the incorporation of elemental Te as an additive in Li-S cells has been shown to enhance Li-metal anode performance. However, in previous studies, Te was primarily employed in the cathode, while the initial step of its mechanism involved Te dissolving in the electrolyte to form lithium polytellurosulfides. The fact that Te particles have limited contact with the electrolyte means a considerable portion of the Te remains inaccessible in the cell. Thus, an electrolyte soluble form of Te may be helpful to further unlock the potential of this system. Since the functional products Li_2TeS_3 and polytellurosulfides both have limited solubility in ether-based electrolytes, moderately soluble $LiTe_3$ is studied and used in a battery, for the first time.

While $LiTe_3$ is usually produced by solid-state reactions that require high temperatures, we present a one-step solution-based reaction to synthesize the electrolyte-soluble lithiated tellurium additive $LiTe_3$, as shown in **Figure 1**a. Commercial Te powder was added into a reducing agent solution in DOL/DME (1:1 volume ratio), as detailed in the experimental section. Three different reducing agents were tested: $LiBH_4$, $LiAlH_4$, and LiH. $LiAlH_4$ can easily reduce Te to insoluble Li_2Te rather than $LiTe_3$ (Figure S1a), and the reaction product AlH_3 is difficult to remove. Meanwhile, $LiBH_4$ produces too much Li_2Te or Te as impurities (Figure S1b and c). For these reasons, LiH was chosen to be the reducing agent to synthesize $LiTe_3$.

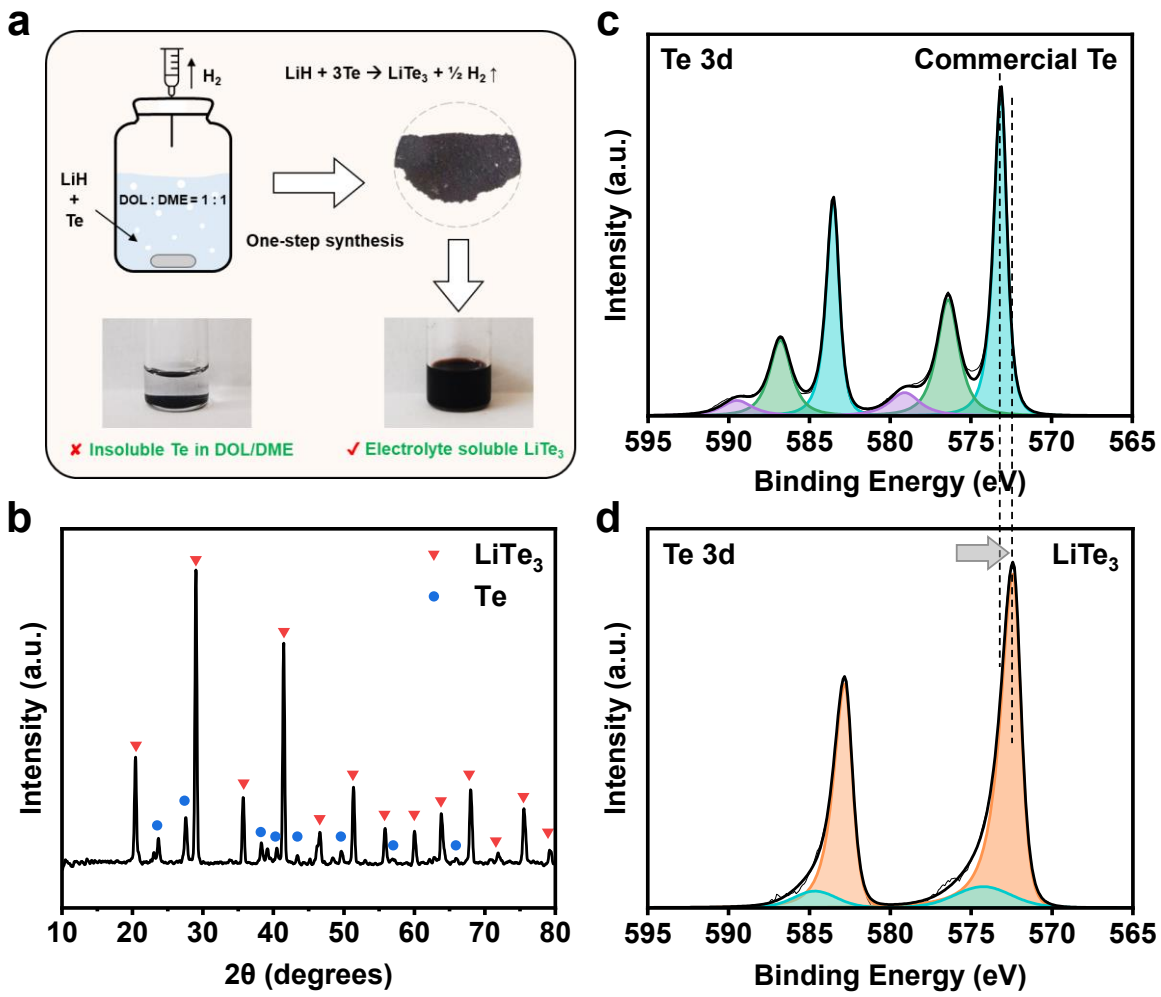

Figure 1. (a) Schematic showing the synthesis process of $LiTe_3$ and its solubility in DOL/DME. (b) XRD pattern of the synthesized $LiTe_3$. Te 3d XPS spectrum for (c) commercial Te powder and (d) synthesized $LiTe_3$.

X-ray diffraction (XRD) and X-ray photoelectron spectroscopy (XPS) data were collected to investigate the chemical structure of the synthesized product. **Figure 1**b shows the XRD pattern, which clearly confirms the existence of $LiTe_3$ and small quantities of unreacted Te. Moreover, the Te 3d spectra for the commercial Te powder and the synthesized $LiTe_3$ demonstrate the successful reduction of Te and a single chemical state for Te in $LiTe_3$, as shown in **Figure 1**c – d. The peak at 573.1 eV corresponds to Te^0, while the peaks at 576.4 and 579.1 eV are associated with TeO_2 and its satellite peak, indicating a partial oxidation present in the

commercial Te powder. In contrast, the vanishing of the Te^0 and Te^{+4} peaks and the emergence of a new peak at 572.5 eV indicates that Te has the expected valance state (-1/3) in $LiTe_3$.

2.2 Electrochemical performance

The influence of the electrolyte additive $LiTe_3$ on the electrochemical performance was evaluated through different cell configurations. To determine the optimized concentration of $LiTe_3$ additive in the electrolyte, cycling performances were tested in anode-free Ni||Li_2S full cells with 0.05, 0.1, and 0.2 M of $LiTe_3$ in the standard electrolyte (1 M LiTFSI + 0.25 M $LiNO_3$) (Figure S2). With similar initial capacities, the one with 0.05 M $LiTe_3$ shows a lower capacity retention after 100 cycles at C/5 rate (~ 57%), while the cells with 0.1 M and 0.2 M $LiTe_3$ retain 71% and 73% of their initial capacities, respectively. The similar capacity retentions between the latter two concentrations indicate similar effects of anode protection and kinetic improvement. This might be due to the robust enough SEI forming on the lithium surface with certain amount of Te in the system. From this data, 0.1 M was chosen to be the concentration of the $LiTe_3$ additive in this study to have a balance among cell performance, energy density, and cost.

Utilizing no excess of lithium in the cell, anode-free full cell is an effective tool for investigating the anode stability and cycling performance.[30, 31] As shown in **Figure 2**a, the anode-free Ni||Li_2S full cell with the standard electrolyte exhibits an initial capacity of 426 mA h g^{-1}, of which only 23% remains after 100 cycles at C/5 rate. There is an average of 3.3 mA h g^{-1} capacity loss per cycle with an average Coulombic efficiency of 96.37% (Figure S3) between the 2^{nd} and 100^{th} cycles at C/5 rate. In contrast, the Ni||Li_2S cell with $LiTe_3$ additive shows a ~ 15% higher initial capacity and a much slower capacity fade (1.4 mA h g^{-1} or 0.29% per cycle). A high specific capacity of ~ 350 mA h g^{-1} is maintained after 100 cycles at C/5 rate with a high Coulombic efficiency of 97.53% (between the 2^{nd} and 100^{th} cycles at C/5 rate),

suggesting excellent lithium plating and stripping efficiency and stability during cycling. It should be noted that blade cast cathodes were used in the cells without any extra conductive materials except those in the slurry, which makes the cell closer to practical cell conditions. Moreover, Ni||Li_2S full cell with a higher loading was also tested (Figure S4). It shows an initial capacity of 507 mA h g^{-1} at a C/5 rate (with four formation cycles at a C/10 rate) and a capacity retention of 70%, which matches quite well with the moderate loading cell mentioned before. In addition, to further demonstrate the capability of $LiTe_3$ additive in protecting the Li anode, electrolytes without $LiNO_3$ were tested in Ni||Li_2S full cells (Figure S5). $LiNO_3$ plays an important role in Li–S batteries for stabilizing lithium deposition, facilitating the redox reactions, and mitigating the shuttle effect.[25, 32] Even in the absence of $LiNO_3$, the cell with $LiTe_3$ additive shows a much better cyclability and a higher capacity compared to the control cell. It retains a capacity above 200 mA h g^{-1} for more than 90 cycles at C/5 rate, while the control cell only lasts 3 cycles before the capacity drops below 200 mA h g^{-1}. The cell with the additive shows a charge-discharge voltage profile with no obvious LiPS shuttling. The small plateau at around 2.6 V may imply the migration of polytellurosulfides to form a protection layer on lithium surface.

Additionally, Li||Li_2S half cells were assembled and assessed to further understand the impact of $LiTe_3$ additive on the cathode side. With a large amount of excess lithium, the lithium loss in the system is compensated, so that the influence of lithium cycling efficiency can be isolated. Figure 2b shows the electrochemical performance of Li||Li_2S cell with and without $LiTe_3$ additive. The capacity retention of the Li||Li_2S cell with $LiTe_3$ additive after 200 cycles at C/5 rate is 65.8% (only an average of 0.17% capacity drop per cycle), while the control cell displays a 45.9% capacity retention. Here, the capacity retention difference is not as significant as that in anode-free cells due to the lithium reservoir at the anode. Still, the cell with $LiTe_3$ additive shows a higher capacity in the 1st cycle at C/5 rate (614 mA h g^{-1}) and after 200 cycles

(404 mA h g^{-1}), while the control cell displays only 562 mA h g^{-1} in the beginning and 258 mA h g^{-1} after 200 cycles. This implies that $LiTe_3$ may improve the kinetics of sulfur species conversion and elevate active material utilization, which will be discussed in detail in the following sections.

Furthermore, to test the cell under more practical lean electrolyte conditions, anode-free pouch full cell was assembled with an electrolyte to Li_2S (E/S) ratio of 5. As depicted in Figure 2c, the cell with the conventional electrolyte exhibits rapid failure, retaining only 70% of its initial capacity after 6 cycles and 24% after 60 cycles. In contrast, the cell incorporating the $LiTe_3$ additive displays stable cycling and maintains 70% of the initial capacity for more than 60 cycles. It is worth noting that in the coin cell, less Te was introduced into the cell compared to our previous study. In the pouch cell, with a lower E/S value, the amount of Te in the system is even lower, suggesting a high utilization of Te with this additive. Additionally, a high Li_2S loading cell with an E/S of 7 was tested (Figure S6). The cell showed good rate performance even with a loading of 7.4 mg cm^{-2}, and was able to maintain an areal capacity > 4 mA h cm^{-2} after 35 cycles.

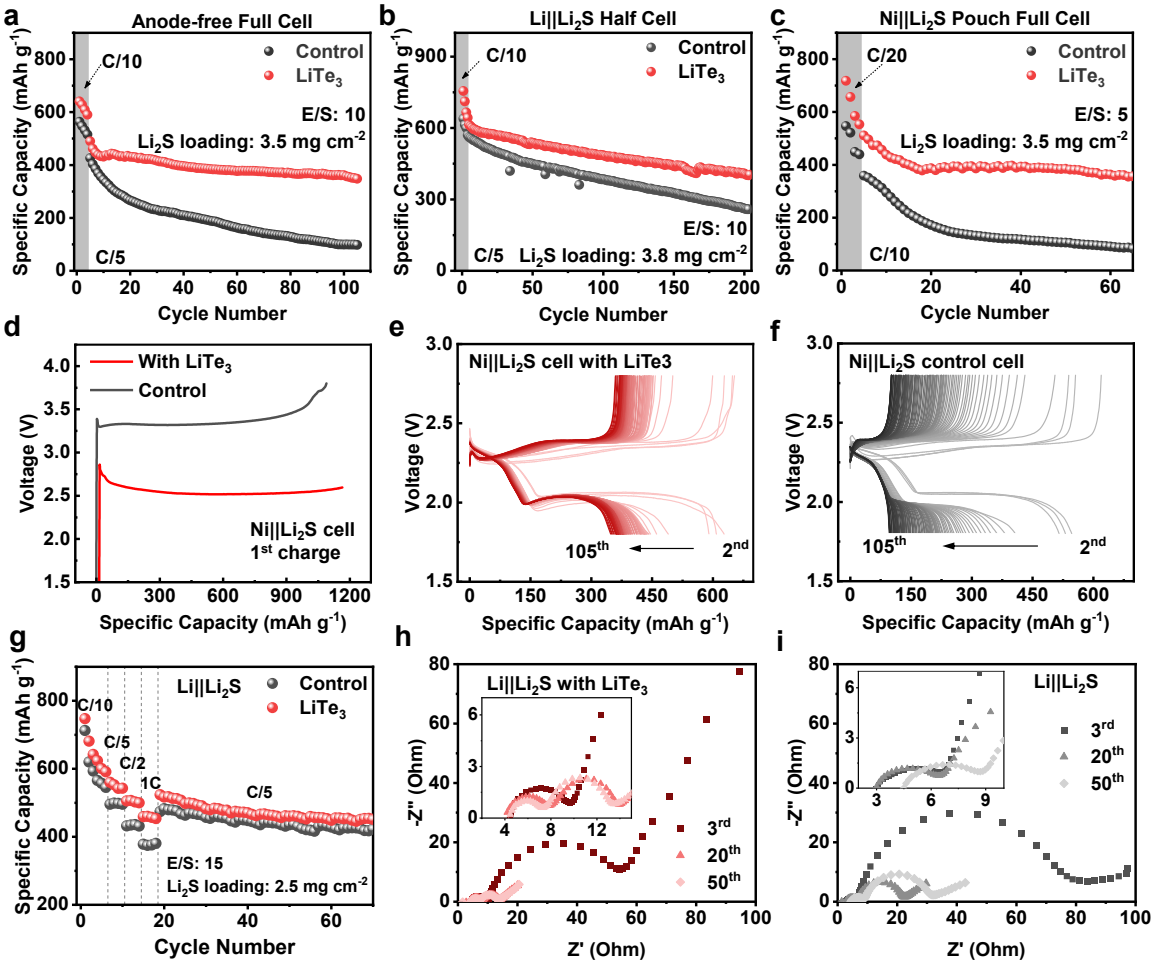

Figure 2. Impact of $LiTe_3$ on the electrochemical performance. Cycling performance of (a) Ni||Li_2S full cell and (b) Li||Li_2S half cell with $LiTe_3$ additive at C/5 rate (with four formation cycles at C/10 rate); (c) cycling performance of Ni||Li_2S pouch full cell with $LiTe_3$ additive at C/10 rate; (d) first charge curves of Ni||Li_2S cell with $LiTe_3$ additive at C/10 rate; charge/discharge voltage profiles of (e) Ni||Li_2S cell with $LiTe_3$ additive and (f) Ni||Li_2S cell with standard electrolyte between 2nd and 105th cycles (2nd to 4th formation cycles at C/10 rate); (g) rate performance of the Li||Li_2S cell with $LiTe_3$ additive at different C rates; Nyquist plots of (h) Li||Li_2S cell with $LiTe_3$ additive and (i) Li||Li_2S cell with standard electrolyte after different cycles.

To better understand the electrochemical activity of $LiTe_3$ in the cell, Li||$LiTe_3$ cells were cycled in different voltage ranges. As shown in Figure S7, when cycling between 1.8 and 2.8 V (same voltage range for the Li_2S cells), the Li||$LiTe_3$ cell displays almost no capacity. When cycling between 1 and 2.8 V, the cell performs like a conventional Li-Te cell, with majority of

its discharge capacity at < 1.7 V. Figure S8 depicts the cyclic voltammetry (CV) plot, showing a similar result. From the left figure, we can see the major cathodic peak at ~ 1.65 V with a small peak at ~ 1.75 V. However, when pairing together with Li_2S_6, the cell displays the typical cyclic voltammograms for Li-S cells with an additional peak at ~ 2.4 V. These results indicate that the improved electrochemical performance is not due to the contribution of capacity from $LiTe_3$ itself, but the alteration of the electrochemical process by the additive.

Moreover, Figure 2d shows that during the initial charging step of the anode-free Ni||Li_2S full cells, $LiTe_3$ additive can lower the charging plateau from ~ 3.3 to ~ 2.5 V, indicating a lower activate barrier and overpotential.[33, 34] The $LiTe_3$ in the electrolyte may have the catalyst effect to facilitate the conversion from Li_2S to soluble polysulfides. Te is assumed to incorporate into the polysulfide chain to form polytellurosulfides as a redox mediator. Additionally, galvanostatic charge and discharge voltage profiles of the Ni||Li_2S cells (with and without $LiTe_3$ additive) from 2nd to 105th cycles are shown in Figure 2e and f. Compared to the control cell, the cell with 0.1 M $LiTe_3$ in the electrolyte exhibits lower and more stable overpotentials, as well as a much slower capacity fade. The rapid decline of the length of the second plateau in the control cell implies severe lithium loss and polysulfide shuttling.

Figure 2g illustrates the rate performance of Li||Li_2S half cell with $LiTe_3$ additive. The cells with the additive continuously deliver stable and reversible capacities at different cycling rates, which are consistently higher than that of the control cell. Even at 1C rate, the cell can still have a discharge capacity of 459 mA h g^{-1}, while the control cell only shows 378 mA h g^{-1}. Furthermore, the cells with the additive can also recover its capacity after the rate goes back to C/5 and keep cycling steadily. Therefore, the redox kinetics and cathode stability are strongly improved with $LiTe_3$ additive, which will be further discussed in section 2.3. Figure 2h and i depict the electrochemical impedance spectroscopy (EIS) results for the Li||Li_2S cell with and without $LiTe_3$ additive. The measurement was carried out on cells in the charged state after

different cycles. Nyquist plots of these cells after cycling consist of two semi-circles at high to medium frequency region and a slope at low-frequency region, which can be ascribed to the electrode-electrolyte surface resistance (R_e), charge transfer resistance (R_{ct}), and Wartburg resistance (W_c), respectively.[35, 36] One can clearly see that R_{ct} significantly decreases after cycling for both cells, which may be a result of cathode wetting and increasing concentration of soluble polysulfide species.[37] Nevertheless, R_{ct} of the cell with $LiTe_3$ additive is noticeably less than that of the control cell, whether after 3, 20, or 50 cycles. The impedance response is almost identical at the 20th and 50th cycle for the cell with the additive, while for the control cell, R_{ct} starts to grow as the cycling continues. This might be due to the formation of a Te-rich SEI that has a higher ionic conductivity when $LiTe_3$ additive is present in the cell, which will be further discussed in section 2.4.

2.3 Effect on the cathode

The fact that $LiTe_3$ additive is soluble and electrochemically active in the electrolyte suggests it may be more likely to interact with the species in the cell and have the unique ability to participate in the sulfur redox reactions, which could lead to better cathode kinetics. To understand this, multiple different techniques were employed, including rate-dependent cyclic voltammetry (CV), Li_2S nucleation study, and operando XRD.

Figure 3a and 3b depicts the rate-dependent CV measurements for Li||S half-cells with and without $LiTe_3$ additive in the electrolyte, respectively. The cell with $LiTe_3$ additive exhibits sharper and stronger redox peaks compared to the control cell, especially for the cathodic peaks at around 2.0 V (C_2), which relate to the liquid-solid transition of sulfur species. The C_2 peak of the control cell starts to split into two peaks, indicating sluggish electrochemical kinetics and slow charge transfer. The difference between the redox peaks becomes more prominent when performing the CV scan with higher sulfur loading cells. As shown in Figure S9, at a scan rate

of 0.1 mV s^{-1}, the control cell shows unstable redox reactions and large polarization between the anodic and cathodic peaks, while the cell with $LiTe_3$ additive still shows a normal CV curve at a low scan rate. Tafel slopes for different steps of sulfur species conversion were fitted and calculated from CV scans of higher loading cells. As shown in Figure S10, the cell with the additive shows lower Tafel slope (75.0 and 71.5 mV dec^{-1}) than the control cell (175.7 and 80.7 mV dec^{-1}) for the Li_2S_n to Li_2S and Li_2S to Li_2S_n conversion. Furthermore, the activation energies (E_a) calculated based on the Tafel plots show a 39 kJ mol^{-1} decrease for Li_2S_n to Li_2S conversion, and an 8.8 kJ mol^{-1} decrease for Li_2S to Li_2S_n conversion, suggesting that the conversion rates are enhanced with the addition of $LiTe_3$.[38, 39] The aforementioned results imply $LiTe_3$ additive, as a redox mediator forming polytellurosulfide with LiPS, can ameliorate redox kinetics for sulfur species. Meanwhile, for the rate-dependent CV curves, the power-law relationship between the measured peak current (i_p) and scan rate (v) can be written as: $i_p = av^b$, where b has a positive relation to the Li^+ diffusion kinetics.[40, 41] By plotting $log\ i_p$ vs. $log\ v$ for the anodic peak (A) and two cathodic peaks (C_1, C_2), b for each set of peaks can be obtained from the slope (Figure 3c and Figure S11). The b yielded from C_2 peaks for the cell with $LiTe_3$ additive is 0.52, compared to 0.27 for the control cell. The significant increase in the b value indicates improved diffusion kinetics and a process that is closer to a fast surface-controlled mechanism, reconfirming the ability of the additive to enhance liquid-solid redox kinetics.

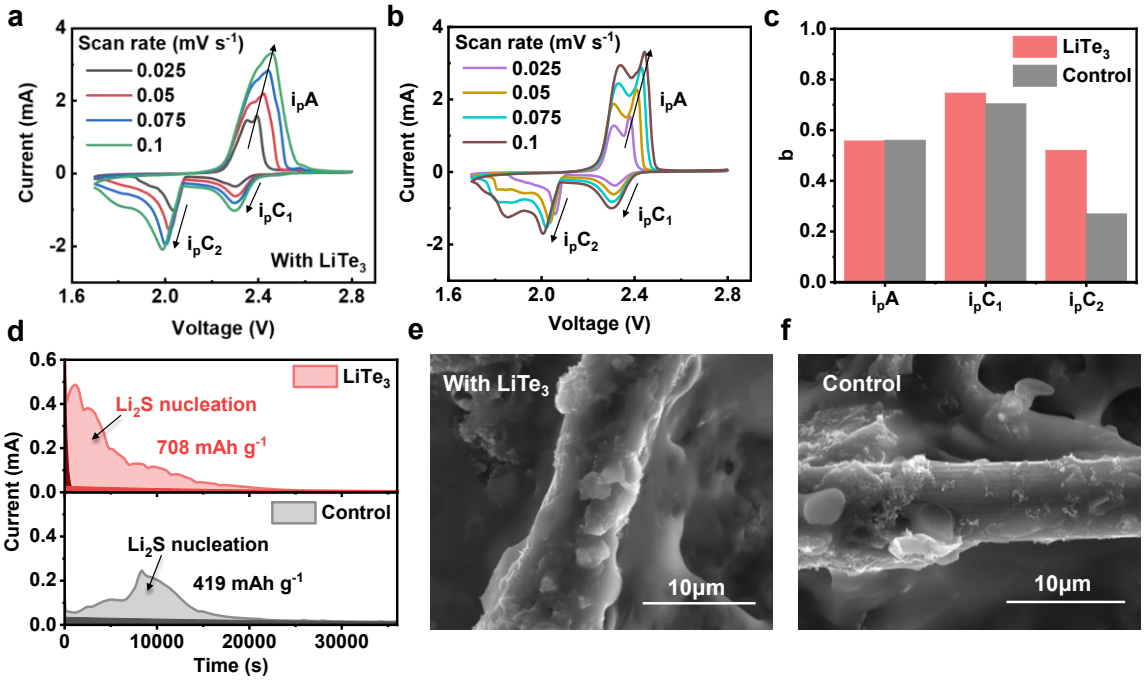

Figure 3. CV curves of the (a) control cell and (b) cell with $LiTe_3$ additive at different scan rates (from 0.025 to 0.1 mV s^{-1}); (c) the slope *b* obtained from plotting log i_p vs. log *v*. (d) Potentiostatic profiles of Li_2S_8/tetraglyme solution discharged to 2.05 V on a carbon paper with and without $LiTe_3$ additive; (e, f) corresponding SEM images of deposited Li_2S on carbon paper with and without $LiTe_3$ additive.

A Li_2S nucleation study (potentiostatic discharge experiment) was performed to further investigate the liquid-to-solid sulfur conversion kinetics.[42, 43] Figure 3d shows the chronoamperometry curves for Li||Li_2S_8 cells. The cell with $LiTe_3$ additive takes less than 1,200 s to reach its peak response current, clearly faster than the control cell that takes > 8,000 s. The cell with the additive also displays a higher peak current (0.49 mA) and larger Li_2S precipitation capacity (708 mA h g^{-1}) compared to the control cell (0.24 mA and 419 mA h g^{-1}). Additionally, the SEM image shows a smooth and complete coverage of Li_2S on carbon fibers for the cell with the $LiTe_3$ additive (Figure 3e and Figure S12). In contrast, the control cell exhibits less and non-uniform precipitated Li_2S deposition (Figure 3f). There are scattered small particles and exposed fibers, indicating worse Li_2S nucleation and growth. CV tests for Li_2S_6 symmetric cells were also carried out. As shown in Figure S13, the cell with $LiTe_3$ exhibits higher redox

current, indicating enhanced liquid-liquid conversion kinetics of the sulfur species. These results demonstrate that $LiTe_3$ can effectively improve the reaction kinetics, lower surface polarization, and capture and interact better with LiPS (matching the cycling performance improvement mentioned in the previous section). The better conductivities of Te-containing species, including Li_xTe_y and $LiTe_xS_y$, could also facilitate Li_2S growth and help increase the utilization of active materials.

Operando XRD was performed to further investigate the kinetics of sulfur redox reactions and better elucidate the relationship between the structure and electrochemical performance in the presence of $LiTe_3$ additive. Operando XRD has been proven to be a great tool for observing sulfur species conversions during the operation of cells.[44, 45] Unlike the conventional Li||S cell, for operando XRD, a Li||Li_2S cell configuration was employed here to better imitate the cell environment of those for the electrochemical tests, especially for the cathode side. As shown in **Figure 4**, the cell with $LiTe_3$ additive displays a significantly lower first charge plateau at ~ 2.5 V compared to the control cell (~ 3.2 V) when activating the Li_2S, as well as more stable discharge profiles and less overpotential. These results are consistent with those mentioned in the previous sections.

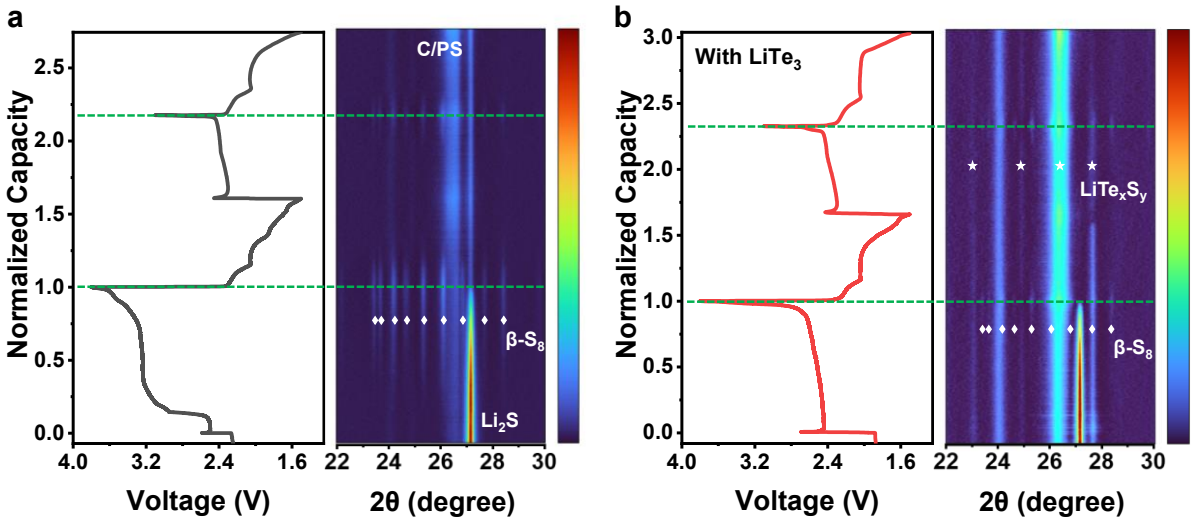

Figure 4. Operando XRD measurements of Li||Li_2S batteries with contour plots on the right and the corresponding voltage profiles on the left. (a) Standard electrolyte and (b) with $LiTe_3$ additive. β-S_8 and Te-related species are represented by diamond and star symbols, respectively.

The peak shown in the contour plots at ~ 27° is attributed to crystalline Li_2S. The cell with $LiTe_3$ additive displays a complete conversion of Li_2S as the Li_2S signal disappears and β-S_8 signals arises at the end of the first charge step. In sharp contrast, for the control cell, there is always a clear Li_2S peak throughout the two cycles, indicating a lower utilization of Li_2S compared to the cell with the additive. Interestingly, for the cell with $LiTe_3$ additive, the peak from Li_2S can barely be detected even when discharged to 1.6 V and having a typical two-plateau voltage profile. This phenomenon suggests the formation of an amorphous or low-crystalline discharge product, which can lead to a lower energy barrier for ionic transfer, better reversibility, and higher utilization of active material.[28, 46, 47] This trend may also be applied to the charge product, as the cell with $LiTe_3$ additive shows relatively weak but more stable β-S_8 signals during two cycles, while the control cell shows rapidly fading peaks, implying a more reversible cycling process with $LiTe_3$ additive. Moreover, the peaks at ~ 23°, 25°, and 28° in Figure 4b may be assigned to Te-containing species, including Te, Li_2Te, and Li_2TeS_3 (Figure S14). The peak at ~ 26° is attributed to carbon in the cathode, LiPS, and Li polytellurosulfides. These extra peaks in the cells with $LiTe_3$ additive confirm the electrochemical activity of $LiTe_3$ in the system, suggesting the formation of polytellurosulfides or Te-related interface layer, which in turn could benefit the anode side.

2.4 Effect on the anode

In Li-S batteries, due to the formation of an unstable SEI layer from LiPS decomposition and severe side reactions with the electrolyte, Li is quickly degraded and irretrievably lost during plating and striping. In the Li-limited anode-free Ni||Li_2S cell (N/P ratio of 1), Li loss is

the main factor of capacity fade as no excess of Li is presented. In this work, with $LiTe_3$ as an electrolyte additive, a more stable and conductive SEI layer is formed and Li deposition is stabilized, leading to a significant improvement in the cyclability of anode-free Ni||Li_2S cell, as mentioned in the previous discussion.

To examine the reactivity of $LiTe_3$ additive in the cell and its mechanism of stabilizing the SEI layer, we reacted a slightly excess amount of $LiTe_3$ with 0.02 M Li_2S_6 solution in DOL/DME. As shown in Figure S15, the color of the solution quickly became darker and changed from bronze (of polysulfide) to red as $LiTe_3$ dissolved and then reacted with Li_2S_6 to form polytellurosulfide species. We could also observe that a precipitate started to form after $LiTe_3$ was added. After standing for 2 h, the color of the red solution became lighter and a clear red precipitation was observed on the walls of the vial, implying that $LiTe_3$ was consumed to precipitate out as Li_2TeS_3. The solution was then examined with UV-vis spectrometry, as shown in Figure S16. The peak for $S_3^{\cdot-}$ radical vanished compared to the plot for Li_2S_6 solution, confirming the reaction between $LiTe_3$ and polysulfides. Furthermore, Ni||Li half cells were assembled to understand the effect of the additive on the Li plating and stripping process, while isolating the influence from the cathode. By adding $LiTe_3$ + Li_2S_6 into the standard electrolyte, the overall Coulombic efficiency improved from 96.8% to 98.3% (**Figure 5**a). The overpotential when plating and stripping Li is also significantly lowered from ~ 12 mV for the control cell to ~ 6 mV for the cell with the additive, consistent with the EIS results mentioned before. Figure 5b shows the morphology of Li deposition (on Ni foil anode) after stripping and plating for 10 cycles. The control cell has a scattered and non-uniform Li surface. In sharp contrast, the cell with the additive allows the formation of smoother and denser Li deposition with larger grains. Similarly, the ability of the additive to stabilize Li plating can also be observed in anode-free full cells. Even after 30 cycles, the anode from the cell with $LiTe_3$

additive still shows a smooth surface and coarse Li grains, while the control cell displays dendritic Li morphology (Figure S17).

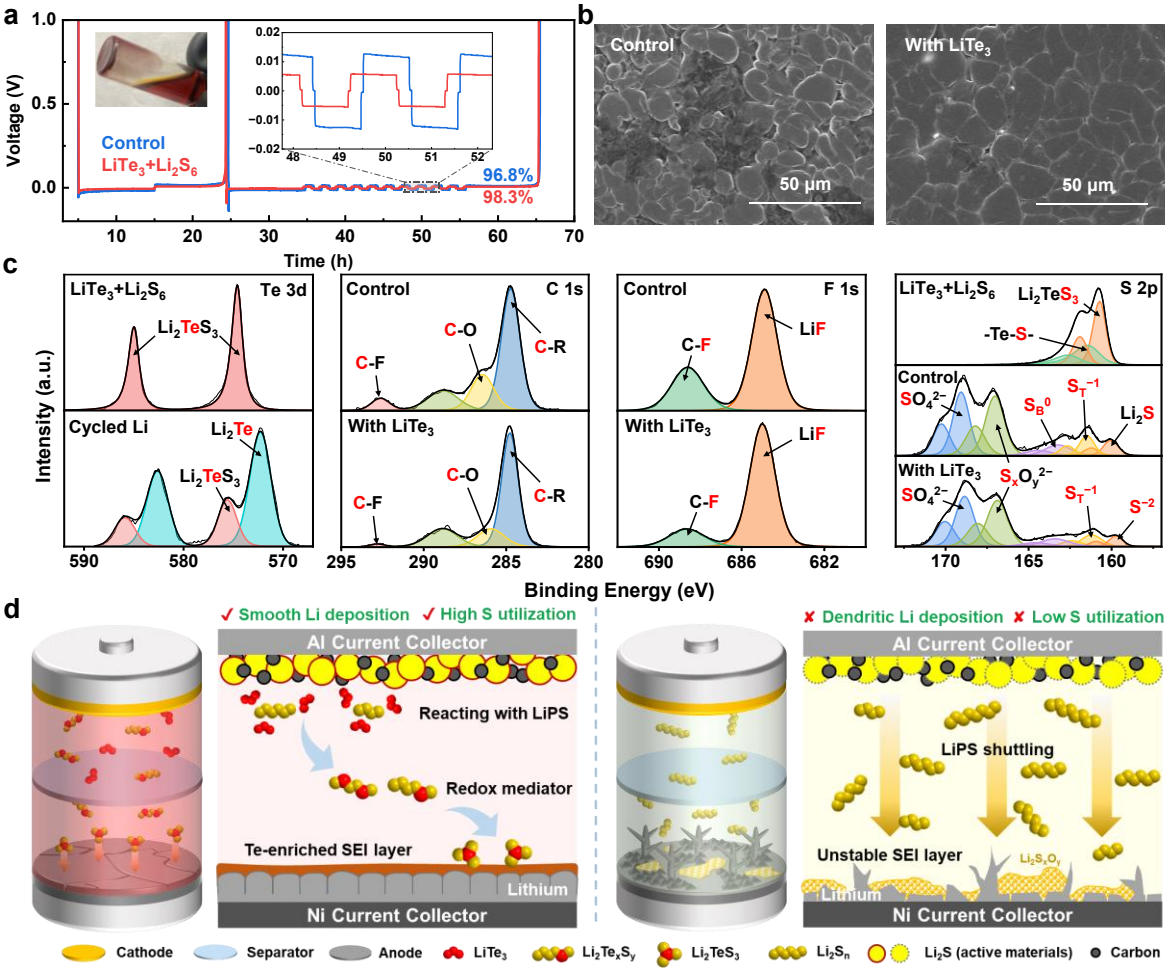

Figure 5. (a) Representative voltage profiles of Ni||Li cells with and without $LiTe_3$ additive for measuring the average CE and overpotential (zoomed in) at 0.5 mA cm^{-2}. (b) SEM images of the Li deposited on Ni from Ni||Li cells with and without the $LiTe_3$ additive. (c) XPS data for the reaction product of $LiTe_3$ + Li_2S_6 and the cycled Ni from Ni||Li cells with and without the $LiTe_3$ additive. (d) Schematic illustration of the working mechanism of anode-free lithium-sulfur cells with and without $LiTe_3$ additive, showing the influence of $LiTe_3$ on Li deposition and cathode kinetics.

XPS measurements were performed on the cycled anodes recovered from the Ni||Li cells and on the reaction products of $LiTe_3$ and Li_2S_6 to further understand the composition of the SEI layer on Li surface (Figure 5c). Regarding the reaction mixture of $LiTe_3$ and Li_2S_6, the Te

3d spectra reveal a single peak at 574.6 eV ($3d_{5/2}$) for Te in +4 oxidation state bonded with S^{2-}, whereas $LiTe_3$ has a $Te^{-1/3}$ peak at 572.5 eV as shown previously, confirming the formation of Li_2TeS_3 from the reaction of $LiTe_3$ and Li_2S_6. The S 2p spectra depict multiple reduced S peaks, including a S^{-2} peak at 160.7 eV ($2p_{3/2}$) corresponding to S in Li_2TeS_3 and a sulfur peak at 161.4 eV ($2p_{3/2}$) for the sulfur atoms in polytellurosulfides (-Te-S-). Compared to the S 2p spectrum for polysulfide (Figure S18), the S atoms are reduced, showing that S oxidized Te to form polytellurosulfides and Li_2TeS_3.

On the other hand, for the cycled anode, the Te 3d spectrum mainly consists of two parts. The Te^{+4} peak at higher binding energy is attributed to Li_2TeS_3 / Li_2TeO_3 as an important protective layer of the anode surface, which can be observed on the cycled Li surface and the separator (Figure S19**)**.[21] The other reduced Te peak can be assigned to $LiTe_x$ (x = 0.5 to 3), which is also a component of the SEI layer. Additionally, in the S 2p spectra, similar line shapes can be observed for the anode samples from both the control cell and the cell with the additive, displaying the oxidized and reduced sulfur species in the SEI layers. However, differences related to the SEI quality can be observed between the two plots. For instance, the peak at ~167 eV is less intense in the spectrum for $LiTe_3$ additive cell, suggesting that the electrochemical inactive thiosulfate and sulfate species are present to a lesser extent.[48] Moreover, in the reduced S region, the three peaks at 159.5 to 163.5 eV are attributed to bridging sulfur (S_B^0), terminal sulfur (S_T^{-1}) in LiPS and polytellurosulfides, and S^{-2} peak (in Li_2S and Li_2TeS_3).[49] The intensity of the S_B^0 peak is lower in the spectrum for the cell with the additive, due to the substitution of Te when forming the polytellurosulfides species. Additionally, the C 1s and F 1s spectra suggest less electrolyte salt and solvent decomposition on the anode with the presence of $LiTe_3$, as the C-F and C-O peaks are clearly less intense than those for the control cell.[50, 51]

Overall, the improved Li stripping/plating Coulombic efficiency and deposited Li morphology in the SEM images show that the Li anode is well protected with the help of the

$LiTe_3$ additive in the Li-S system. This stems from the formation of a high-quality Te-containing SEI with fewer unfavorable species, as the XPS and other characterization results suggest.

3. Conclusion

We presented, for the first time, $LiTe_3$ as a novel electrolyte additive for Li-S batteries. The additive was synthesized with commercial Te with a one-step reduction process. $LiTe_3$ could regulate the reaction chemistry for both the anode and cathode to significantly improve the cyclability of anode-free Li-S cells. Specifically, at the cathode, $LiTe_3$ quickly reacts with LiPS to form lithium polytellurosulfides and Li_2TeS_3, which act as redox mediators to significantly lower the activation barrier for Li_2S in the first cycle, promote the conversion of sulfur species, and facilitate the precipitation of Li_2S. The sulfur utilization is noticeably increased with the help of this additive. Meanwhile, the migration of the generated Te-containing species to the anode introduces a Li_2TeS_3/Li_2Te-enriched SEI layer on Li surface. Li morphology and its plating/stripping efficiency indicate that this interphase layer is more stable and conductive, so effective to achieve reversible Li deposition.

With only 0.1 M concentration in the conventional DOL/DME-based electrolyte, the $LiTe_3$ additive helps retain 71% of the capacity in anode-free full-cell after 100 cycles (350 mA h g^{-1}), while the control has only 23% left (< 100 mA h g^{-1}). Even in an anode-free pouch cell with a lean electrolyte condition, the cell with the additive realizes a stable operation and greatly outperforms the control cell (60 cycles versus 8 cycles for 70% retention). The significantly improved specific capacity and its retention in the anode-free configuration cells prove the ability of $LiTe_3$ additive to remarkably enhance the performance of both the cathode and anode. Moreover, this additive has the potential to be applied to other electrolyte systems for Li-S cells

and provides a new strategy to design electrolyte additives for boosting the performance of metal-sulfur batteries.

4. Experimental Methods

Synthesis of $LiTe_3$: $LiTe_3$ was prepared by a solution-based reaction. 0.2 M lithium hydride (LiH, Sigma Aldrich) was dispersed in a 1:1 volume ratio of 1,3-dioxalane (DOL, Sigma Aldrich) and 1,2-dimethoxyethane (DME, Sigma Aldrich). 0.6 M tellurium powder (Te, Sigma Aldrich) was then added to the solution. The mixture was stirred for three to five days to get a dark red solution. The solvent was then removed to obtain the $LiTe_3$ powder (dark grey color). All the synthesis processes were performed inside an Ar-filled glovebox. Needles and glass vials with septum on the cap were used to release the pressure from the containers.

Electrode Preparation: Li_2S cathode was prepared by a slurry blade-cast method. Lithium sulfide (Li_2S, 70 wt%, Alfa Aesar), super P (10 wt%), carbon nanofibers (CNF, 10 wt%), and binder (10 wt% of solid) were milled in a PTFE bottle by a roll jar-milling system for 48 h at 70 rpm. The 4 wt% binder solution was prepared by dissolving polyethylene oxide (PEO, average MW ~ 4,000,000, Sigma Aldrich) and polyvinylpyrrolidone (PVP, average MW ~ 1,300,000) in a 4:1 wt. ratio in acetonitrile. DME and 1,4-dioxane were added in a 1:1 volume ratio as the slurry medium. The overall solid content was controlled at 15 – 17 wt%. 5 mm and 8 mm yttria-stabilized zirconia (YSZ) grinding balls (Advanced Materials) were used to uniformly mix the slurry. The slurry was then doctor-blade cast onto carbon coated Al-foil with different thickness and dried in vacuum for 24 h. The electrodes were punched into 7/16-inch diameter discs, and had a Li_2S loading of 2.5 – 4.5 mg cm^{-2}. For the high-loading cell, the Li_2S slurry was dropped onto a carbon paper and dried.

The sulfur cathode was prepared for the CV measurement by a similar blade-cast method. Sulfur-Ketjenblack (S/KB, 90 wt% S) composite (75 wt%), super P (10 wt%), CNF (10 wt%),

and PEO/PVP binder (10 wt% of solid) were mixed to get a slurry by a Thinky mixer. The slurry was then doctor-blade cast and dried to get electrodes with a S loading of 2 – 4 mg cm^{-2}.

Electrochemical Measurements: Anode-free Ni || Li_2S full cells and Li || Li_2S half cells were assembled with CR2032 cell cases in an Ar-filled glovebox for electrochemical measurements. Ni foil was cut in 9/16-inch diameter discs as the current collectors for anode-free Ni || Li_2S full cells, while lithium chips were used as the anodes for Li || Li_2S half cells. One layer of Celgard 2500 separator was used in each cell. The standard electrolyte used consists of 1 M LiTFSI (Sigma Aldrich) + 0.25 M lithium nitrate ($LiNO_3$) in a DOL/DME (1:1, volume ratio) cosolvent. To prepare the electrolyte with the additive, 0.1 M (or 0.05 M) $LiTe_3$ was added to the standard electrolyte. The E/S (electrolyte to Li_2S) ratio was controlled to be 10 μL mg^{-1} unless otherwise mentioned. Cells were rested for 10 h before cycling. The galvanostatic cycling tests were performed at C/10 rate for 3 cycles and then at C/5 rate between 2.8 and 1.8 V. The upper limit for the initial charging step was 3.8 V. Ni || Li cells were assembled for the CE tests with Ni foil and Li chip on each side. Standard electrolyte, electrolyte with 0.1 M $LiTe_3$, and electrolyte with 0.1 M $LiTe_3$ and 0.2 M Li_2S_6 were used in the cells. CE was determined by a modified method as previously reported.[52] Li was initially plating on the Ni foil for 10 h at a current density of 0.5 mA cm^{-2} and fully stripped to 1 V at the same current density. Then, 0.5 mA h of Li was plated and stripped for 10 cycles to obtain the CE. Cyclic voltammetry (CV) tests were conducted on a Biologic VMP-3 system in the potential range of 2.8 to 1.8 (or 1.2) V. EIS measurements were performed in the frequency range of 1 MHz to 10 mHz. All the cell cycling data were collected with a Land (CT3002A) or an Arbin battery testing system.

Li_2S Nucleation Study: 0.2 M Li_2S_8, 1 M LiTFSI, and 0.25 M $LiNO_3$ in DOL/DME (1:1 volume ratio) was used as catholyte, while the electrolyte without Li_2S_8 was used as anolyte. $LiTe_3$ (0.002 mmol, 20 μL 0.1 M solution) was dropped onto a commercial carbon paper

(Avcarb) and dried. 20 μL of catholyte and anolyte were dropped on the carbon paper and lithium chip anode. The assembled cells were discharged galvanostatically at 89 μA to 2.15 V and then potentiostatically discharged at 2.05 V until the current was less than 0.01 mA.

Li_2S_6 Symmetric Cell Assembly: 0.2 M Li_2S_6, 1 M LiTFSI, and 0.25 M $LiNO_3$ in DOL/DME (1:1 volume ratio) was used as electrolyte. $LiTe_3$ (0.001 mmol, 10 μL 0.1 M solution) was dropped onto carbon papers and dried. The symmetric cell was assembled with two identical loaded carbon papers as the electrodes, and 20 μL of Li_2S_6 electrolyte on each side.

Pouch Cell Assembly and Testing: Anode-free pouch full cells were fabricated with Ni foil anode and Li_2S cathode. The cathodes were punched into 5.6 × 4.3 cm (~24 cm^2) sheets, while the anodes had a slightly larger dimension (5.8 × 4.5 cm). Standard electrolyte and electrolyte with 0.1 M $LiTe_3$ were used to make the cells. The E/S ratio was controlled to be 5 μL mg^{-1}. The pouch cells were put in pressure holders to ensure a uniform pressure. The cells were cycled at C/20 rate for 4 formation cycles between 1.7 and 2.8 V with a 3.8 V voltage limit for the first charging step, before cycling at C/10 rate between 1.7 and 2.6 V for the rest of the test.

Materials Characterization: Powder X-ray diffraction was performed with a Rigaku MiniFlex 600 Diffractometer to study the crystalline structure of materials. *Operando* XRD analysis was performed on a Rigaku Ultima IV X-ray diffractometer with a specially designed cell. Li_2S slurry was dropped onto a beryllium disk and dried inside the glovebox overnight to make the cathode. The cell was cycled between 1.6 and 3.0 V (except the first charge step to 3.8 V) at C/20 rate for two cycles. SEM images were obtained with a FEI Quanta 650 ESEM to study the morphology of the samples. A Cary 5000 spectrophotometer was used to collect UV-vis absorption spectra. A Kratos X-ray Photoelectron Spectrometer with monochromatic Al Kα radiation was used for XPS analysis. Samples were transferred with an air-tight chamber to the instrument. Anodes and cathodes from the disassembled cells were rinsed with DME and

dried inside the glovebox to make the SEM and XPS samples. For solution-based XPS samples, the solution was dropped on bucky papers and then dried inside the glovebox.

Supporting Information

Supporting Information is available from the Wiley Online Library or from the author.

Acknowledgements

This work was supported by the National Science Foundation, Division of Chemical, Bioengineering, Environmental, and Transport Systems, under award number 2011415. The authors would like to thank Dr. Hugo Celio, Dr. Biyu Jin, Dr. Yuxun Ren and Hyunki Sul for insightful discussions and assistance with XPS, operando XRD, and other experiments.

Received: ((will be filled in by the editorial staff))
Revised: ((will be filled in by the editorial staff))
Published online: ((will be filled in by the editorial staff))

References

[1] A. Manthiram, Y. Fu, S. Chung, C. Zu, Y. Su, *Chem. Rev.* **2014**, *114*, 11751.

[2] S.-H. Chung, C.-H. Chang, A. Manthiram, *Adv. Funct. Mater.* **2018**, *28*, 1801188.

[3] A. Bhargav, J. He, A. Gupta, A. Manthiram, *Joule* **2020**, *4*, 285.

[4] G. Zhou, H. Chen, Y. Cui, *Nat. Energy* **2022**, *7*, 312.

[5] L. Hou, X. Zhang, B. Li, Q. Zhang, *Mater. Today* **2021**, *45*, 62.

[6] X.-Y. Li, S. Feng, M. Zhao, C.-X. Zhao, X. Chen, B.-Q. Li, J.-Q. Huang, Q. Zhang, *Angew. Chem., Int. Ed.* **2022**, *61*.

[7] B. Jin, Y. Li, J. Qian, X. Zhan, Q. Zhang, *ChemElectroChem* **2020**, *7*, 4158.

[8] J. Xiang, W. Shen, Z. Guo, J. Meng, L. Yuan, Y. Zhang, Z. Cheng, Y. Shen, X. Lu, Y. Huang, *Angew. Chem.* **2021**, *133*, 14434.

[9] W. Yao, J. Xu, L. Ma, X. Lu, D. Luo, J. Qian, L. Zhan, I. Manke, C. Yang, P. Adelhelm, R. Chen, *Adv. Mater.* **2023**, 2212116.

[10] T. Feng, T. Zhao, N. Zhang, Y. Duan, L. Li, F. Wu, R. Chen, *Adv. Funct. Mater.* **2022**, *32*, 2202766.

[11] W. Qu, Z. Lu, C. Geng, L. Wang, Y. Guo, Y. Zhang, W. Wang, W. Lv, Q. Yang, *Adv. Energy Mater.* **2022**, *12*, 2202232.

[12] L. Wang, W. Hua, X. Wan, Z. Feng, Z. Hu, H. Li, J. Niu, L. Wang, A. Wang, J. Liu, X. Lang, G. Wang, W. Li, Q.-H. Yang, W. Wang, *Adv. Mater.* **2022**, *34*, 2110279.

[13] J. He, A. Bhargav, A. Manthiram, *Angew. Chem., Int. Ed.* **2022**, *61*.

[14] D. Guo, F. Ming, D.-B. Shinde, L. Cao, G. Huang, C. Li, Z. Li, Y. Yuan, M.-N. Hedhili, H.-N. Alshareef, Z. Lai, *Adv. Funct. Mater.* **2021**, *31*, 2101194.

[15] Y.-X. Yao, X.-Q. Zhang, B.-Q. Li, C. Yan, P.-Y. Chen, J.-Q. Huang, Q. Zhang, *InfoMat* **2020**, *2*, 379.

[16] Y. Ren, Z. Cui, A. Bhargav, J. He, A. Manthiram, *Adv. Funct. Mater.* **2022**, *32*, 2106680.

[17] J. He, A. Bhargav, H. Sul, A. Manthiram, *Angew. Chem.* **2023**, *135*.

[18] Y. Zhao, Y. Ye, F. Wu, Y. Li, L. Li, R. Chen, *Adv. Mater.* **2019**, *31*, 1806532.

[19] J. Xie, S. Sun, X. Chen, L. Hou, B. Li, H. Peng, J. Huang, X. Zhang, Q. Zhang, *Angew. Chem., Int. Ed.* **2022**, *61*, e202204776.

[20] C. Bi, L. Hou, Z. Li, M. Zhao, X. Zhang, B. Li, Q. Zhang, J. Huang, *Energy mater. adv.* **2023**, *4*.

[21] S. Nanda, A. Bhargav, A. Manthiram, *Joule* **2020**, *4*, 1121.

[22] H. Sul, A. Bhargav, A. Manthiram, *Adv. Energy Mater.* **2022**, *12*, 2200680.

[23] M. Zhao, B.-Q. Li, H.-J. Peng, H. Yuan, J.-Y. Wei, J.-Q. Huang, *Angew. Chem., Int. Ed.* **2020**, *59*, 12636.

[24] D. Guo, J. Wang, T. Lai, G. Henkelman, A. Manthiram, *Adv. Mater.* **2023**, 2300841.

[25] S. Nanda, A. Manthiram, *Adv. Energy Mater.* **2021**, *11*, 2003293.

[26] F. Wu, J.-T. Lee, N. Nitta, H. Kim, O. Borodin, G. Yushin, *Adv. Mater.* **2015**, *27*, 101.

[27] Z. Lin, Z. Liu, W. Fu, N.-J. Dudney, C. Liang, *Adv. Funct. Mater.* **2013**, *23*, 1064.

[28] Y. Ren, A. Bhargav, W. Shin, H. Sul, A. Manthiram, *Angew. Chem.* **2022**, *134*.

[29] X. Li, S. Feng, C. Zhao, Q. Cheng, Z. Chen, S. Sun, X. Chen, X. Zhang, B. Li, J. Huang, Q. Zhang, *J. Am. Chem. Soc.* **2022**, *144*, 14638.

[30] S. Nanda, A. Gupta, A. Manthiram, *Adv. Energy Mater.* **2021**, *11*, 2000804.

[31] J. Chen, J. Xiang, X. Chen, L. Yuan, Z. Li, Y. Huang, *Energy Storage Mater.* **2020**, *30*, 179.

[32] H. Chu, J. Jung, H. Noh, S. Yuk, J. Lee, J.-H. Lee, J. Baek, Y. Roh, H. Kwon, D. Choi, K. Sohn, Y. Kim, H.-T. Kim, *Adv. Energy Mater.* **2020**, *10*, 2000493.

[33] Y. Liu, X. Meng, Z. Wang, J. Qiu, *Nat. Commun.* **2022**, *13*.

[34] C. Geng, W. Qu, Z. Han, L. Wang, W. Lv, Q. Yang, *Adv. Energy Mater.* **2023**, *13*, 2204246.

[35] Z. Wang, M. Feng, H. Sun, G. Li, Q. Fu, H. Li, J. Liu, L. Sun, A. Mauger, C.-M. Julien, H. Xie, Z. Chen, *Nano Energy* **2019**, *59*, 390.

[36] Z. Cui, N. Khosla, T. Lai, J. Narayan, A. Manthiram, *ACS Appl. Mater. Interfaces* **2023**, *15*, 1247.

[37] B. Jin, L. Yang, J. Zhang, Y. Cai, J. Zhu, J. Lu, Y. Hou, Q. He, H. Xing, X. Zhan, F. Chen, Q. Zhang, *Adv. Energy Mater.* **2019**, *9*, 1902938.

[38] Z. Li, C. Luo, S. Zhang, G. Sun, J. Ma, X. Wang, Y. He, F. Kang, Q. Yang, W. Lv, *InfoMat* **2022**, *4*, e12361.

[39] C. Zhao, X. Li, M. Zhao, Z. Chen, Y. Song, W. Chen, J. Liu, B. Wang, X. Zhang, C. Chen, B. Li, J. Huang, Q. Zhang, *J. Am. Chem. Soc.* **2021**, *143*, 19865.

[40] X. Huang, Z. Wang, R. Knibbe, B. Luo, S.-A. Ahad, D. Sun, L. Wang, *Energy Technol.* **2019**.

[41] S. Nanda, A. Bhargav, Z. Jiang, X. Zhao, Y. Liu, A. Manthiram, *Energy Environ. Sci.* **2021**, *14*, 5423.

[42] H. Yuan, H. Peng, B. Li, J. Xie, L. Kong, M. Zhao, X. Chen, J. Huang, Q. Zhang, *Adv. Energy Mater.* **2019**, *9*, 1802768.

[43] Z. Li, Y. Zhou, Y. Wang, Y. Lu, *Adv. Energy Mater.* **2019**, *9*, 1802207.

[44] J. Conder, R. Bouchet, S. Trabesinger, C. Marino, L. Gubler, C. Villevieille, *Nat. Energy* **2017**, *2*.

[45] J. He, A. Bhargav, A. Manthiram, *Adv. Mater.* **2020**, *32*, 2004741.

[46] D. Su, D. Zhou, C. Wang, G. Wang, *Adv. Funct. Mater.* **2018**, *28*, 1800154.

[47] H. Noh, J. Song, J. Park, H. Kim, *J. Power Sources* **2015**, *293*, 329.

[48] B. Jin, D. Wang, J. Zhu, H. Guo, Y. Hou, X. Gao, J. Lu, X. Zhan, X. He, Q. Zhang, *Adv. Funct. Mater.* **2021**, *31*, 2104433.

[49] Z. Liu, X. He, C. Fang, L.-E. Camacho Forero, Y. Zhao, Y. Fu, J. Feng, R. Kostecki, P.-B. Balbuena, J. Zhang, J. Lei, G. Liu, *Adv. Funct. Mater.* **2020**, *30*, 2003605.

[50] H. Chu, H. Noh, Y. Kim, S. Yuk, J. Lee, J. Lee, H. Kwack, Y. Kim, D. Yang, H. Kim, *Nat. Commun.* **2019**, *10*.

[51] B. Jin, Z. Cui, A. Manthiram, *Angew. Chem.* **2023**, *135*.

[52] B.-D. Adams, J. Zheng, X. Ren, W. Xu, J.-G. Zhang, *Adv. Energy Mater.* **2018**, *8*, 1702097.

Table of Contents

Synthesized with a simple one-step process, $LiTe_3$ is employed as a novel electrolyte additive for lithium-sulfur batteries. By regulating the reaction chemistry for both the anode and cathode, the additive helps to increase the utilization of active materials, achieve reversible lithium deposition, and improve the cyclability of anode-free lithium-sulfur cells.

*Tianxing Lai, Amruth Bhargav, and Arumugam Manthiram**

Lithium Tritelluride as an Electrolyte Additive for Stabilizing Lithium Deposition and Enhancing Sulfur Utilization in Anode-free Lithium-sulfur Batteries

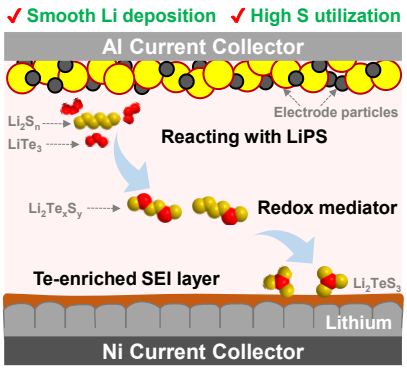

Supporting Information

Lithium Tritelluride as an Electrolyte Additive for Stabilizing Lithium Deposition and Enhancing Sulfur Utilization in Anode-free Lithium-sulfur Batteries

*Tianxing Lai, Amruth Bhargav, and Arumugam Manthiram**

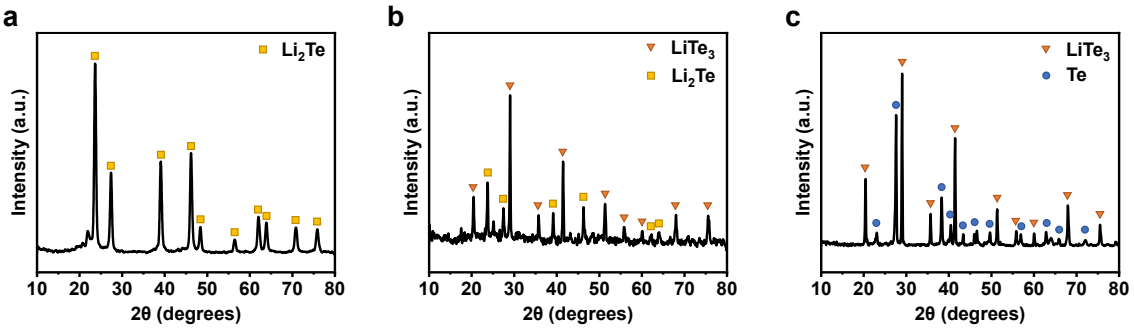

Figure S1. XRD patterns of the synthesized products with (a) 2 $LiAlH_4$ + Te, (b) $LiBH_4$ + Te, and (c) 2 $LiBH_4$ + 3 Te.

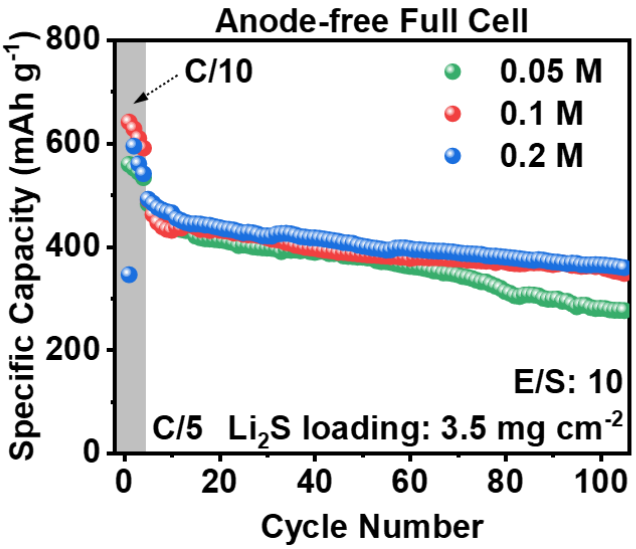

Figure S2. Cycling performance of anode-free Ni||Li_2S full cell at C/5 rate (with four formation cycles at C/10) with different concentrations of $LiTe_3$ additive in the electrolyte.

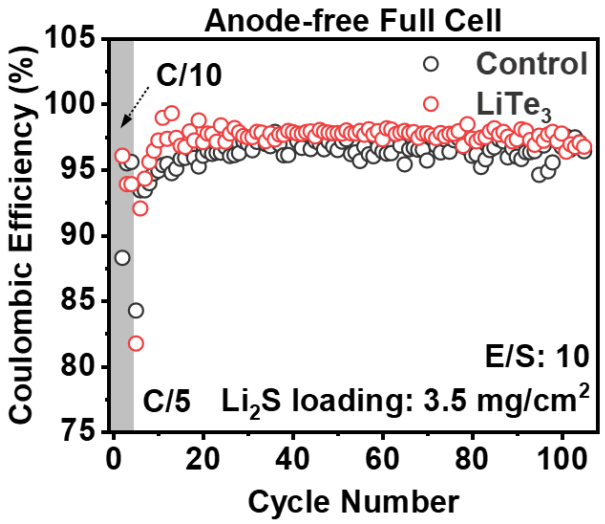

Figure S3. Coulombic efficiency of anode-free Ni||Li_2S full cell at C/5 rate (with four formation cycles at C/10) with the control electrolyte and with 0.1 M $LiTe_3$ additive.

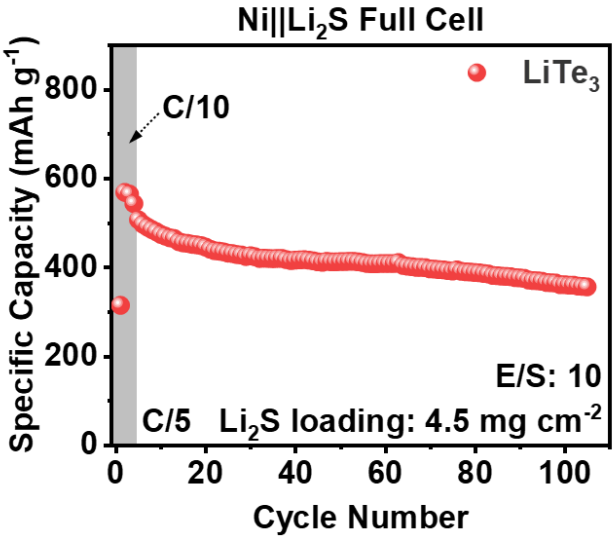

Figure S4. Cycling performance of anode-free Ni||Li_2S full cell at C/5 rate (with four formation cycles at C/10) with a higher Li_2S loading and 0.1 M $LiTe_3$ in the electrolyte.

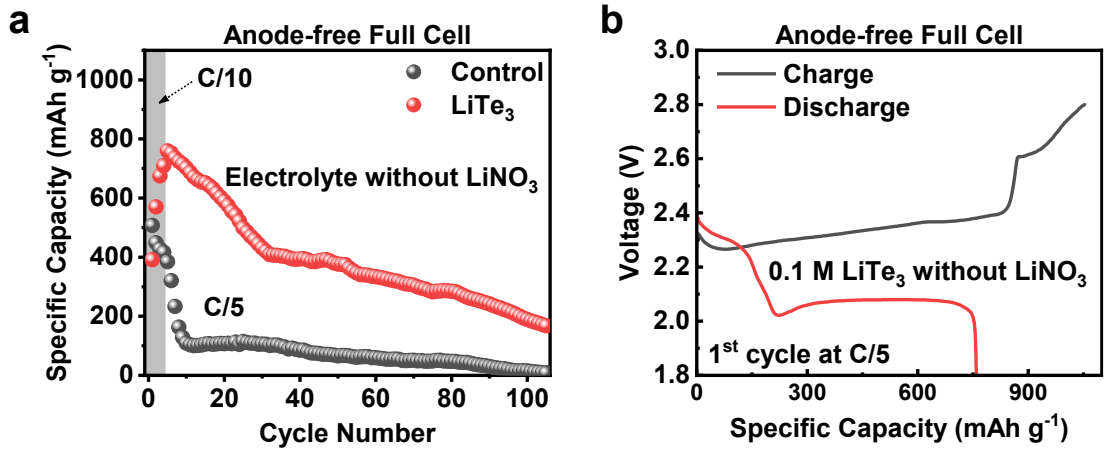

Figure S5. (a) Cycling performance of anode-free Ni||Li_2S full cell with 0.1 M $LiTe_3$ in the electrolyte in the absence of $LiNO_3$; (b) charge/discharge voltage profiles of that cell at 1st cycle at C/5 rate.

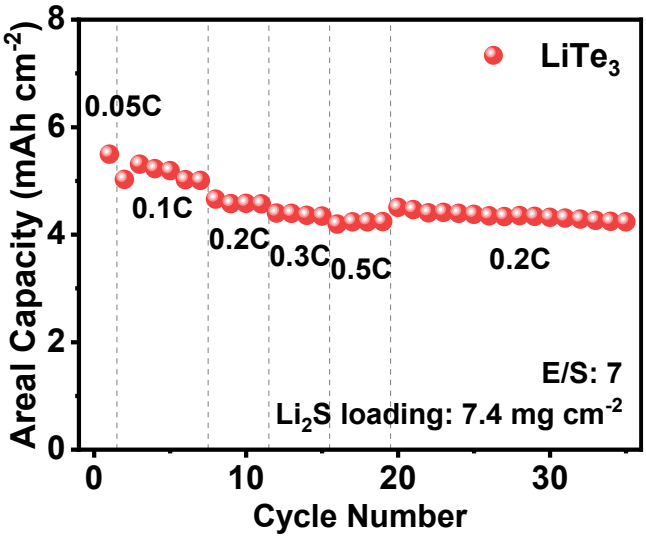

Figure S6. Rate performance of the high-loading Li||Li_2S cell at different current densities.

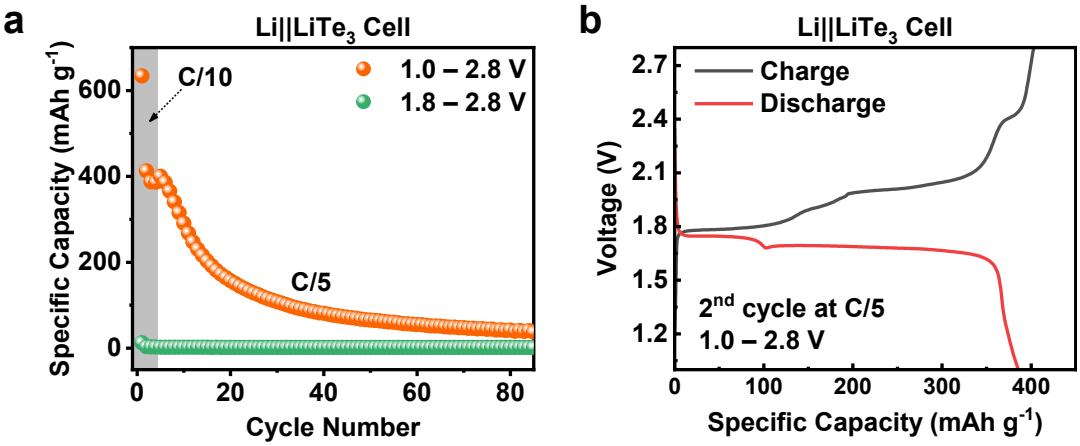

Figure S7. (a) Performance of the Li||$LiTe_3$ cell ($LiTe_3$ as the only active material) when cycling between different voltage ranges; (b) typical charge/discharge voltage profiles of Li||$LiTe_3$ cell (2^{nd} cycle at C/5 rate).

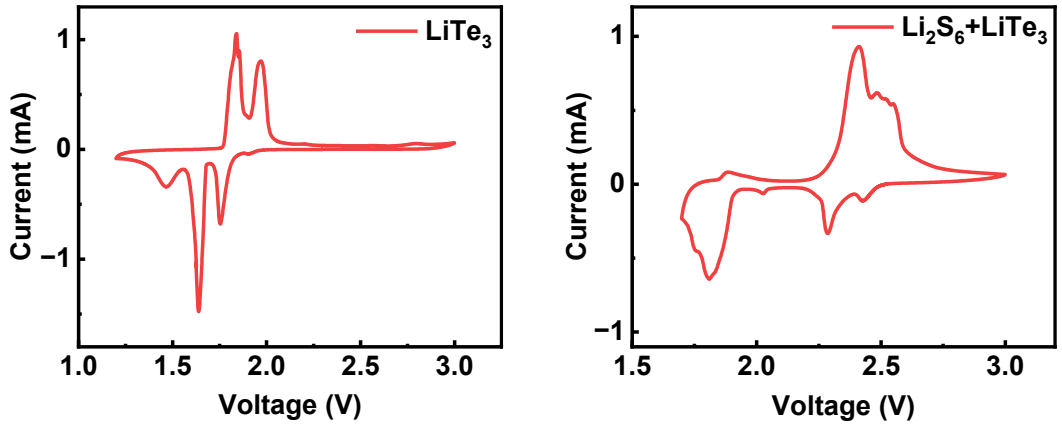

Figure S8. CV curves of $LiTe_3$ additive alone and $LiTe_3$ paired with Li_2S_6.

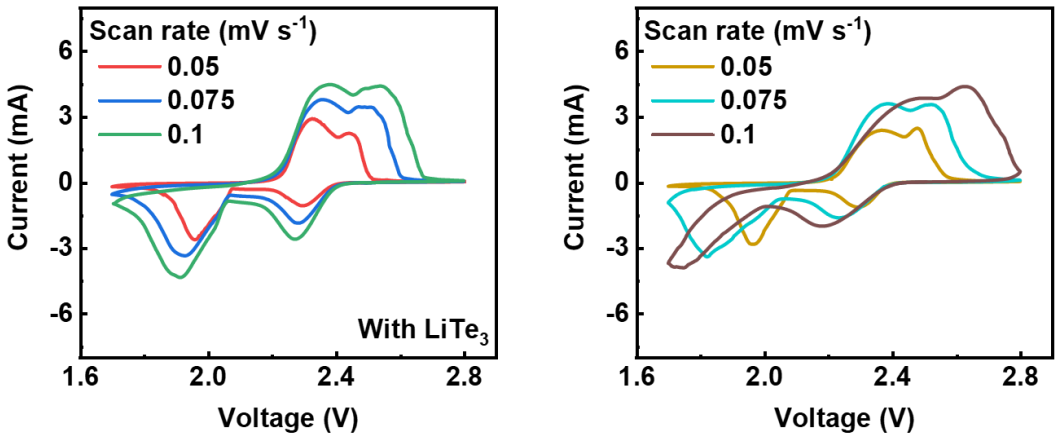

Figure S9. CV curves of Li||S cells with and without $LiTe_3$ additive with a higher loading (3.5 mg cm^{-2}) at different scan rates.

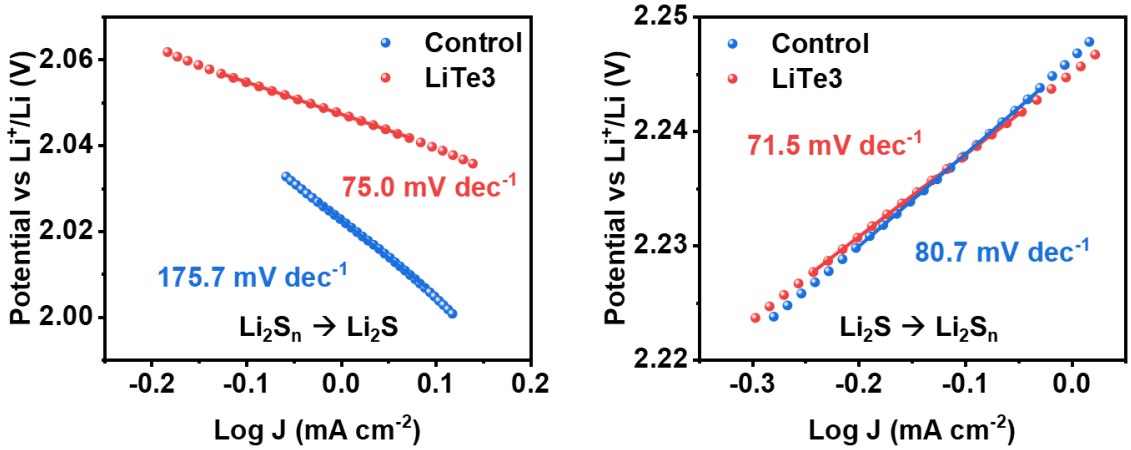

Figure S10. Tafel plots corresponding to the redox reactions of Li_2S_n to Li_2S and Li_2S to Li_2S_n, derived from CV curves for Li-S cells with and without $LiTe_3$ at a scan rate of 0.075 mV s^{-1}.

Calculation of activation energy: The activation energy difference for the sulfur redox process was calculated by the following equation:

$$E_a = E_a^0 - \frac{\ln(10)\,RT}{b}\varphi_{cathode}(Ox|Red)$$

where E_a is the activation energy of the redox process, E_a^0 is the intrinsic activation energy, b is the slope of the Tafel plot (V vs log J), and $\varphi_{cathode}(Ox|Red)$ is the irreversible potential of the redox peaks. We can substrate the two equations for the cells with and without $LiTe_3$ to get the activation energy difference for each step.

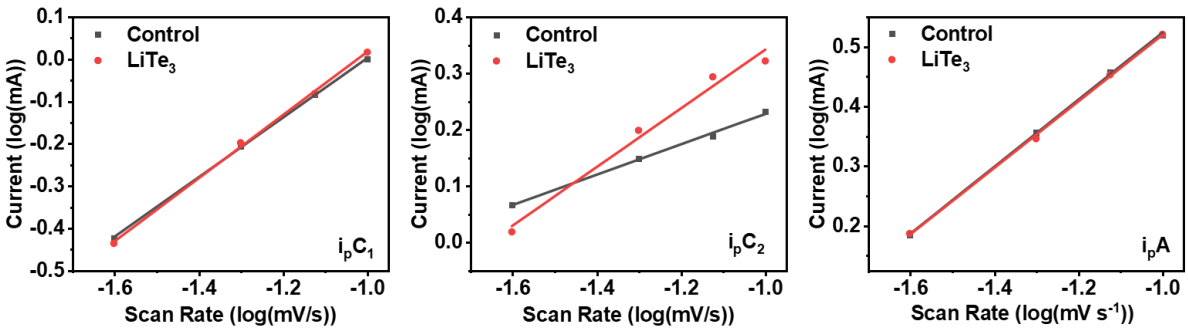

Figure S11. Linear fitting plots of log peak current versus log scan rate for two cathodic peaks, (a) C_1 and (b) C_2, and (c) the anodic peak A.

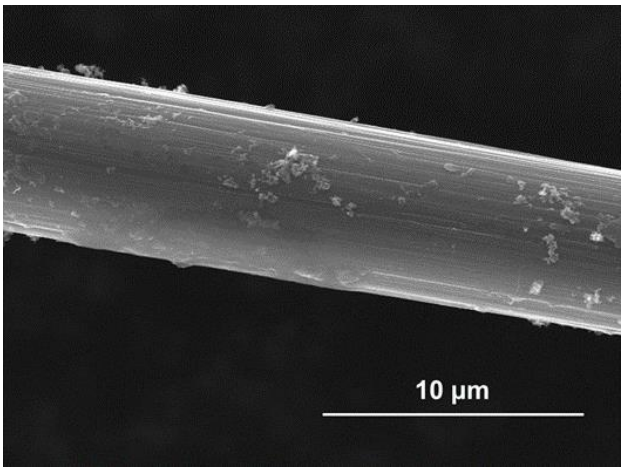

Figure S12. SEM image of pristine carbon paper.

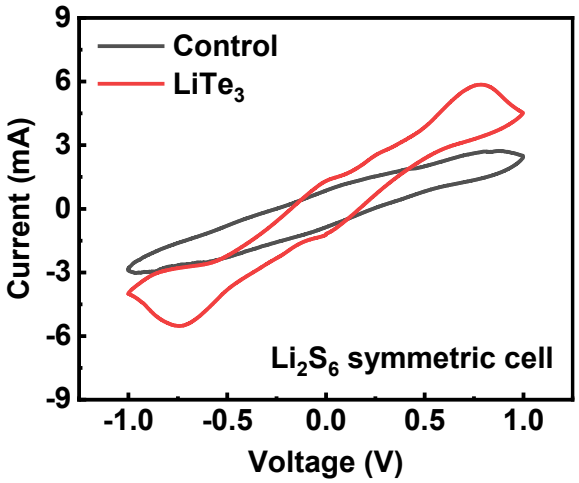

Figure S13. CV curves for Li_2S_6 symmetric cells with and without $LiTe_3$ additive at a scan rate of 5 mV s^{-1}.

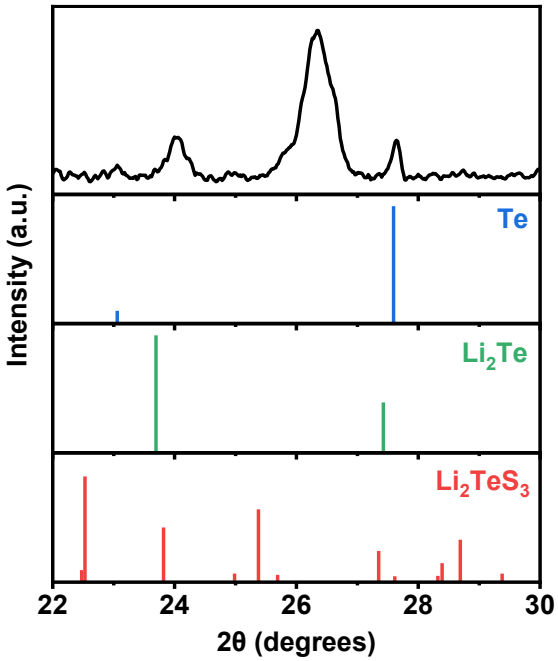

Figure S14. XRD pattern selected from operando XRD measurement at 50% discharged state at the 1st cycle.

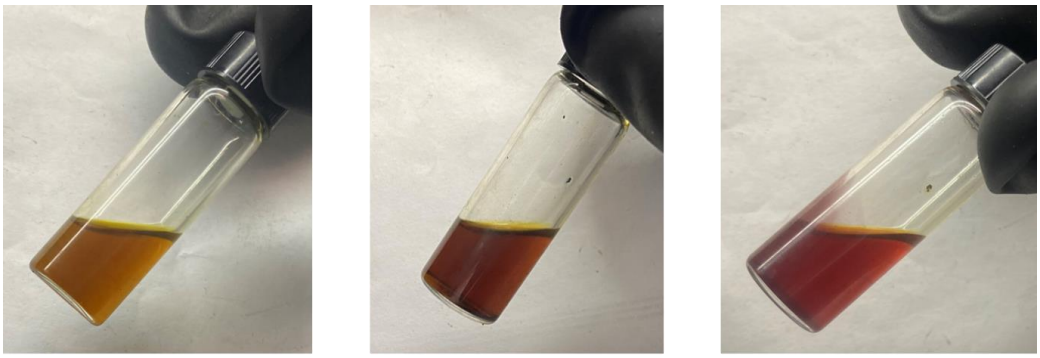

Figure S15. Photos of $LiTe_3$ reacted with Li_2S_6 solution in DOL/DME. From left to right: original 0.02 M Li_2S_6 solution, when $LiTe_3$ was added into the solution, 2 h after $LiTe_3$ was added.

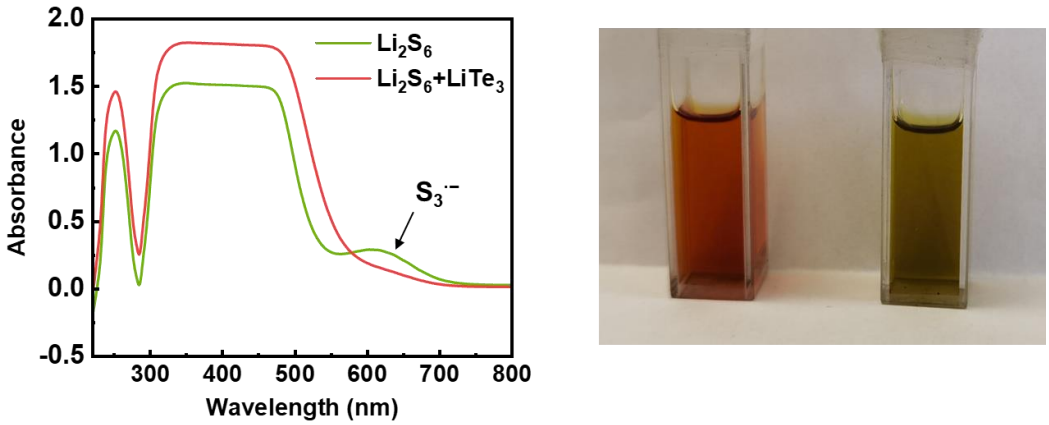

Figure S16. Left: UV-vis absorption spectra of 0.02 M Li_2S_6 solution before and after the addition of $LiTe_3$. Right: Corresponding photos for Li_2S_6 solution before (right) and after (left) the addition of $LiTe_3$.

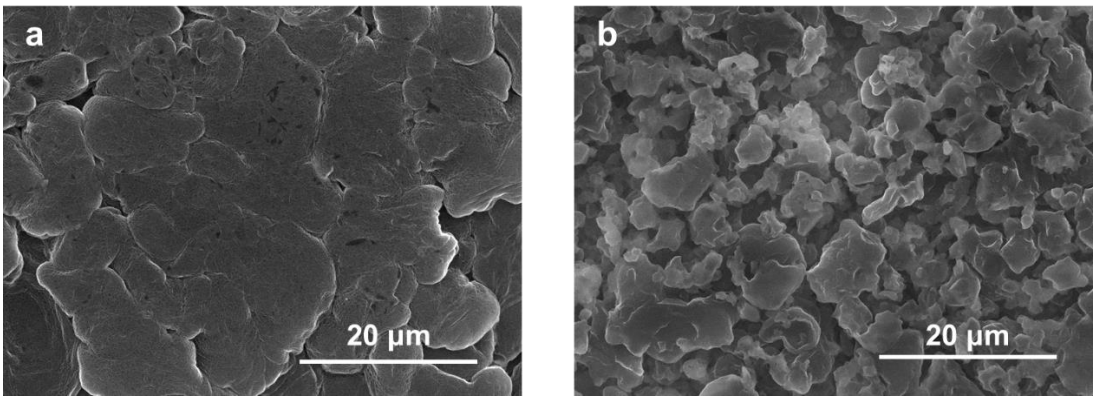

Figure S17. SEM images of charged anode (Li surface on Ni foil) after 30 cycles at C/5 rate, (a) with $LiTe_3$ additive, (b) without LiTe3 additive to the electrolyte (1 M LiTFSI + 0.25 M $LiNO_3$ in DOL/DME).

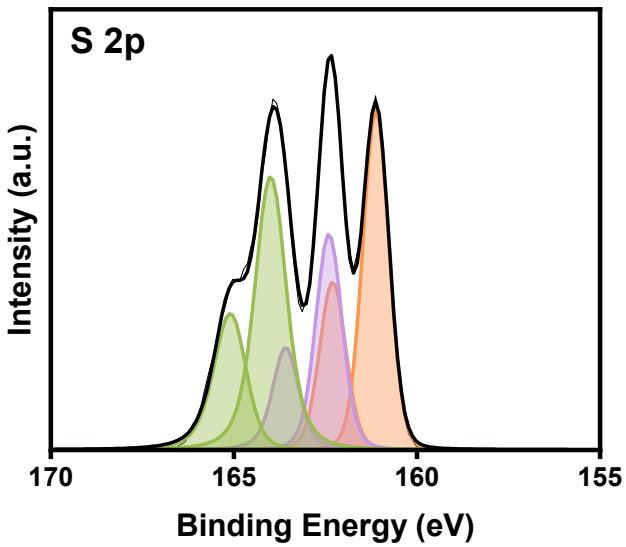

Figure S18. S 2p spectrum for Li_2S_6, where the three peaks ($2p_{3/2}$) are at 161.1, 162.4, and 163.9 eV.

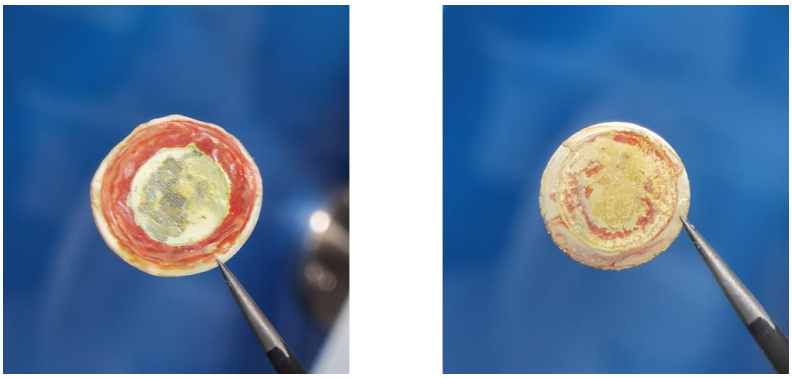

Figure S19. Cycled separator and Li anode disassembled from Ni||Li and Li||Li_2S cells with the $LiTe_3$ additive.